01 Aug 2009

A Novel TDR-Based Coaxial Cable Sensor for Crack/Strain Sensing in Reinforced Concrete Structures

Shishuang Sun

David Pommerenke
Missouri University of Science and Technology, davidjp@mst.edu

James L. Drewniak
Missouri University of Science and Technology, drewniak@mst.edu

Genda Chen
Missouri University of Science and Technology, gchen@mst.edu

et. al. For a complete list of authors, see https://scholarsmine.mst.edu/ele_comeng_facwork/1390

Recommended Citation

S. Sun et al., "A Novel TDR-Based Coaxial Cable Sensor for Crack/Strain Sensing in Reinforced Concrete Structures," *IEEE Transactions on Instrumentation and Measurement*, vol. 58, no. 8, pp. 2714-2725, Institute of Electrical and Electronics Engineers (IEEE), Aug 2009.
The definitive version is available at https://doi.org/10.1109/TIM.2009.2015706

A Novel TDR-Based Coaxial Cable Sensor for Crack/Strain Sensing in Reinforced Concrete Structures

Shishuang Sun, *Member, IEEE*, David J. Pommerenke, *Senior Member, IEEE*, James L. Drewniak, *Fellow, IEEE*, Genda Chen, Liang Xue, *Member, IEEE*, Michael A. Brower, and Marina Y. Koledintseva, *Senior Member, IEEE*

***Abstract*—Novel coaxial cable sensors that feature high sensitivity and high spatial resolution are developed for health monitoring of concrete structures using a time-domain reflectometry (TDR). The new sensor was designed based on the topology change of its outer conductor, which was fabricated with tightly wrapped commercial tin-plated steel spiral covered with solder. The cracks that developed within concrete structures will lead to out-of-contact of local steel spirals. This topology change results in a large impedance discontinuity that can be measured with a TDR. A simplified equivalent transmission line model and numerical full-wave simulations using finite-difference time-domain techniques were used to optimize the sensor design. The sensors under test demonstrated high sensitivity and the capability of multiple-crack detection. A plasma-sprayed coating technique was employed to improve sensor uniformity. Engineering implementation issues, e.g., signal loss, signal postprocessing, and sensor design optimization, were also addressed.**

***Index Terms*—Coaxial cable, crack/strain sensor, plasma spray, sensitivity, signal loss, spatial resolution, time-domain reflectometry (TDR).**

I. Introduction

CRACK detection is one of the primary concerns in health monitoring of civil infrastructures, because cracks may lead to structural degradation. This condition happens due to reinforcement corrosion that is associated with the leakage of water and chloride through cracks. The National Research Board reported that nearly 20% of the bridge structures in the 1995 National Bridge Inventory database were classified as structurally deficient [1].

Traditionally, tens or hundreds of discrete sensors, e.g., strain gauges, accelerometers, and others, are used in the health monitoring of complex civil infrastructures with a vibration-based technique [2], [3]. The cost of sensors and associated wiring, data acquisition, data storage system, and data postprocessing are often significant. Therefore, it is imperative to develop low-cost distributed sensors for damage detection. There are two emerging candidates: 1) a coaxial cable sensor that uses the electrical time-domain reflectometry (TDR) technology and 2) a fiber-optic sensor. A good review of a variety of fiber-optic sensors can be found in [4]. There are several different types of distributed fiber optic sensors [5]–[9]. They share some common features such as geometrical adaptability, very long measurement distance, and high measurement accuracy. The disadvantages are that the fiber-optic measurement instruments are usually very expensive, whereas these sensors are only applicable to quasistatic measurements, and the spatial resolution and sensitivity are comparatively low. Herein, the sensitivity is defined as the smallest crack that a sensor can detect, and the spatial resolution is defined as the minimum distance between two adjacent cracks that can be resolved by a crack sensor. The distributed fiber-optic sensors are good candidates for measuring a slowly varying strain over a long distance. In contrast, coaxial cable sensors with TDR technology feature high spatial resolution, high sensitivity, less expensive instruments, and a real-time measurement capability. Previously, coaxial cable sensors were designed based on the cross-sectional change of a coaxial cable, which resulted in a low sensitivity for structural applications, because the impedance of a coaxial cable is not very sensitive to the cross-sectional change [10]–[12]. However, these sensors still demonstrate better sensitivity than fiber-optic sensors. Another disadvantage of coaxial cable sensors is that the useful length of cable sensors is limited, because the sensitivity and spatial resolution of coaxial cable sensors reduce with the length of cable sensors due to signal loss [13].

One innovative design was proposed to significantly enhance the sensitivity of cable sensors. In this design, the topology (or electrical structure) of a coaxial cable is modified. The outer conductor of the sensor was fabricated with a tightly wrapped commercial tin-plated steel spiral that is covered with solder. The separation of local steel spiral, which results from the cracks that were developed in concrete structures, leads to a large discontinuity that can easily be detected with a TDR.

Manuscript received December 24, 2007; revised June 2, 2008. Current version published July 17, 2009. This work was financially supported in part by the U.S. National Science Foundation (NSF) under Award CMS0200381 and Award CMS0409420. The results, findings, and opinions expressed in this paper are those of the authors only and do not necessarily represent those of the NSF. The Associate Editor coordinating the review process for this paper was Dr. Devendra Misra.

S. Sun is with the Product Characterization Group, Altera Corporation, San Jose, CA 95134 USA (e-mail: ssun@altera.com).

D. J. Pommerenke, J. L. Drewniak, and M. Y. Koledintseva are with the EMC Laboratory, Department of Electrical and Computer Engineering, Missouri University of Science and Technology (formerly University of Missouri-Rolla), Rolla, MO 65409 USA (e-mail: davidjp@mst.edu; drewniak@mst.edu; marinak@mst.edu).

G. Chen is with the Department of Civil, Architectural, and Environmental Engineering, Missouri University of Science and Technology (formerly University of Missouri-Rolla), Rolla, MO 65409 USA (e-mail: gchen@mst.edu).

L. Xue is with the VLSI Department, Nvidia Corporation, Santa Clara, CA 95050-2519 USA (e-mail: liang.xue@nsc.com).

M. A. Brower is with the Burns & McDonnell Engineering Company, Kansas City, MO 64114 USA (e-mail: mabyq9@mst.edu).

Color versions of one or more of the figures in this paper are available online at http://ieeexplore.ieee.org.

Digital Object Identifier 10.1109/TIM.2009.2015706

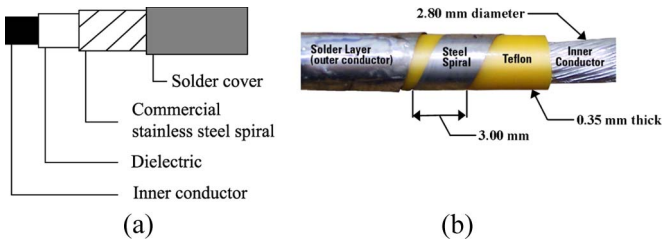

Fig. 1. Crack sensor prototype. (a) Schematic illustration. (b) Photo of a cut-away sensor.

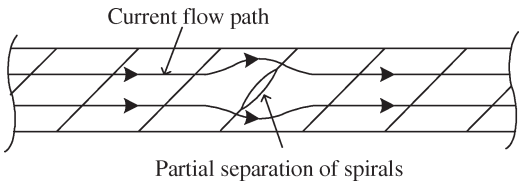

Fig. 2. Schematic illustration of the current flow path with the presence of a separation between adjacent spirals.

In Section II, the sensor prototype, mechanism, and numerical simulations are briefly reviewed. In Section III, the performance of the sensor is demonstrated with experimental measurements. In Section IV, the plasma-sprayed coating technique that aims at sensor automatic fabrication is discussed. In Section V, several engineering implementation issues, e.g., the influence of signal loss on the sensitivity and spatial resolution, sensor design optimization, and signal processing techniques, were addressed. Conclusions are given in Section VI.

II. Cable Sensor Mechanism

One prototype of the crack sensor is schematically illustrated in Fig. 1(a), and a photo of a cut-away sensor is shown in Fig. 1(b). The sensor consists of four components: 1) an inner conductor; 2) a dielectric layer; 3) an outer conductor fabricated with tightly wrapped stainless steel spiral; and 4) a thin solder cover. The stainless steel spiral is tin plated and commercially available. One key factor in the fabrication of this topology-change-based sensor is to ensure that any two adjacent spirals are electrically connected but will easily separate under mechanical loading.

A. Underlying Physics and a Simplified Transmission Line Model

The presence of a partial or complete separation between adjacent spirals in the outer shield of the cable sensor changes the return current flow path on the outer conductor, as illustrated in Fig. 2. This condition results in an added series inductance. This discontinuity causes a portion of an incident wave to reflect back [14]. One simplified equivalent transmission line model is shown in Fig. 3.

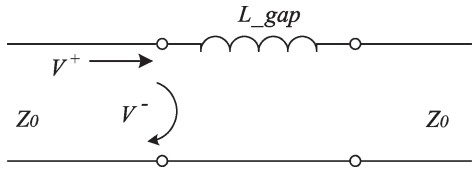

Fig. 3. Equivalent transmission line model of a coaxial cable sensor with a separation between spirals.

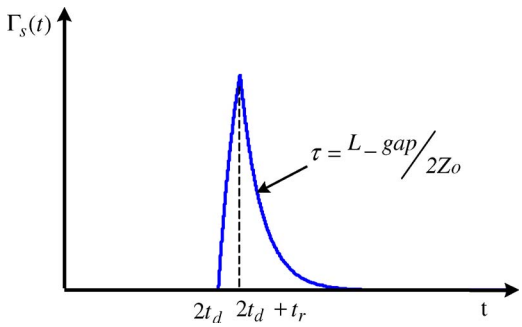

Fig. 4. Waveform of reflection coefficient according to (1).

The relationship between the reflection coefficient at the source end and the added series equivalent inductance L_gap can be derived according to the transmission line theory [14]. When the sensor is excited with a step pulse with a transition duration t_r, the reflection coefficient at the source end Γs can be derived as (1), shown at the bottom of the page [15]. Here, $u(t)$ is a unit-step function, Zo is the characteristic impedance of the cable sensor, and L_gap is the added inductance associated with a gap between adjacent spirals. The wave traveling time from the source to the discontinuity, i.e., a spiral separation, is t_d. The corresponding waveform is shown in Fig. 4. The waveform rapidly rises in a time interval t_r and then exponentially attenuates. The decaying time constant is $\tau = L\_gap/2Z_0$. The reflection coefficient is a function of the added inductance, the characteristic impedance of the cable sensor, and the transition duration of the step pulse. The maximum reflection coefficient occurs at a time instant $t = 2t_d + t_r$ and is

$$[\Gamma_s(t)]_{\max} = \frac{L\_gap}{t_r \cdot 2Z_0} \cdot \left[1 - e^{-(2Z_0/L\_gap)\cdot t_r}\right], \quad t = 2t_d + t_r. \tag{2}$$

As indicated in (2), the maximum reflection coefficient of the sensor is inversely proportional to the characteristic impedance of the sensor.

The value of the added inductance L_gap can be determined with TDR waveforms obtained from either simulations or measurements as [15], [16]

$$L\_gap = \frac{4Z \times A}{V_o} \tag{3}$$

where A is the area underneath a pulse, which is the integration of the pulse over time, and V_o is the peak voltage of the step pulse launched with the TDR.

$$\Gamma_s(t) = \begin{cases} 0, & t_r \le t < 2t_d \\ \frac{L\_gap}{t_r \cdot 2Z_0} \cdot \left\{\left[1 - e^{-(2Z_0/L\_gap)\cdot(t-2t_d)}\right] \cdot u(t-2t_d) - \left[1 - e^{-(2Z_0/L\_gap)\cdot(t-2t_d-t_r)}\right] \cdot u(t-2t_d-t_r)\right\}, & t \ge 2t_d \end{cases} \tag{1}$$

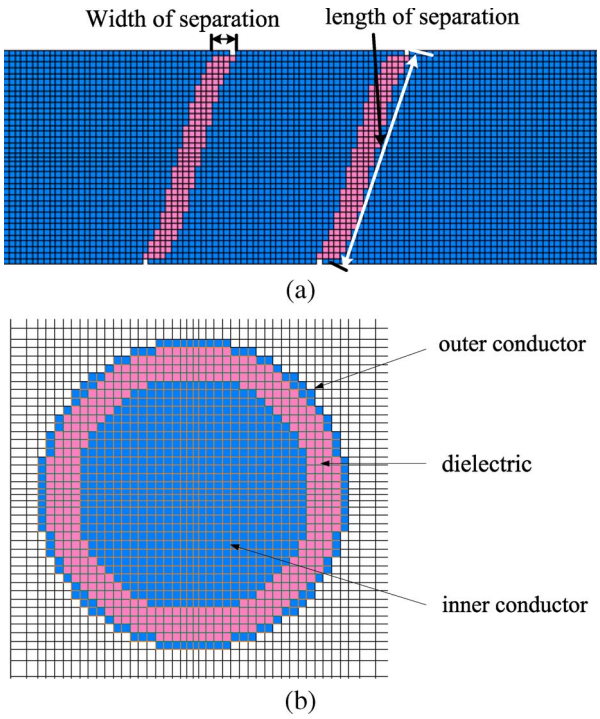

Fig. 5. Meshed FDTD model of a coaxial cable sensor. (a) Side view. (b) Two-dimensional cross-sectional view.

TABLE I
SPIRAL WRAPPED COAXIAL CABLE SENSORS

Sensor	Inner conductor diameter	Outer conductor diameter	Spiral width	Characteristic impedance
I	2.8 mm	3.5 mm	3.0 mm	9.3 Ω
II	2.8 mm	3.5 mm	5.0 mm	9.3 Ω

B. Numerical Simulations

Crack cable sensors were numerically simulated to investigate their response and sensitivity with a commercial finite-difference time-domain (FDTD) full-wave numerical electromagnetic tool. Snapshots of the FDTD models of a sensor are shown in Fig. 5. The inner conductor of the cable sensor was modeled as a round metallic cylinder. For the outer conductor, thin helix wires were accumulated to form tightly wrapped steel spirals. By removing a portion of several helix wires, a small gap can be created to represent a partial separation of spirals caused by the strain/cracks applied on a sensor. The sensor was excited with a coaxial port, which launches a Gaussian pulse with 6-GHz bandwidth for 3-dB attenuation. The port impedance is the same as that of the sensors, which is 9.3 Ω. The voltage waveform that was monitored at the port was integrated over time to obtain TDR waveforms.

Two cable sensor models were simulated. The dimensions and characteristic impedance of the two cable sensors are summarized in Table I. The sensor diameters and the spiral widths were determined based on the commercially available materials. The main difference of the two sensors is their spiral width. Any crack is characterized by the spiral width of separation and the length of separation, as illustrated in Fig. 5(a).

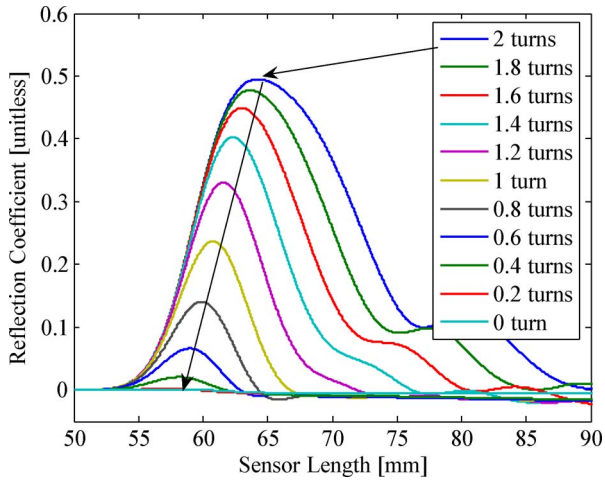

Fig. 6. TDR responses of Sensor I under various lengths of cracking.

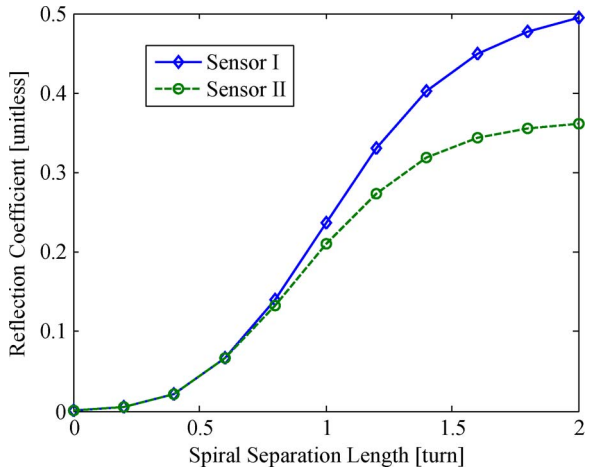

Fig. 7. Peak values of the reflection coefficient with increasing length of spiral separation.

In the simulations of both sensors, variable length and width of spiral separation were used. Herein, the length of separation is expressed with a decimal number of turns. For example, the value of 0.2 turns indicates that the spiral separation is 20% of one complete turn. Fig. 6 shows the simulated TDR waveforms of Sensor I with a fixed separation width of 0.2 mm and different separation lengths from 0.2 to 2 turns, with an increment of 0.2 turns. Fig. 7 illustrates the relationship between the peak values of the reflection coefficient and the length of the spiral separation. According to the figure, the peak values of the reflection coefficient exponentially increase with the separation length when it is less than 0.6 turns. When the length of spiral separation is from 0.6 to 1.4 turns, which is the most likely range for actual crack developing, the peak values of the reflection coefficient increase almost linearly with respect to the length of a spiral separation. Fig. 8 shows that the peak values of the reflection coefficient linearly increase with the increasing width of the spiral separation from 0.2 to 1 mm when the length of spiral separation is fixed (0.6 turns for both sensors). Note that, for an actual crack developing, the width and length of a spiral separation simultaneously increase. To simplify simulations, only one parameter—either the width or the length of spiral separation—is a variable for each set of simulations.

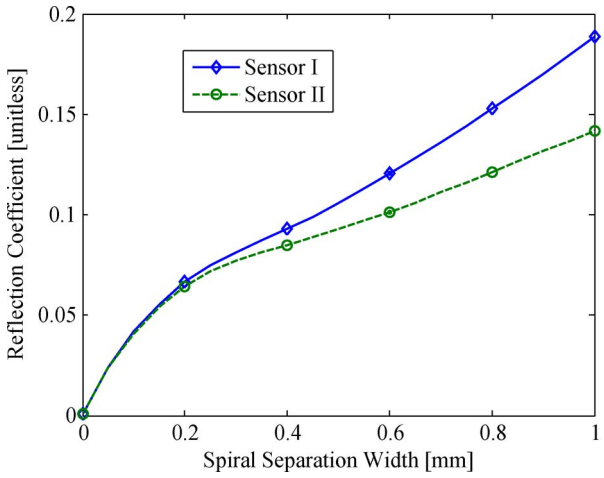

Fig. 8. Peak values of the reflection coefficient with increasing width of spiral separation.

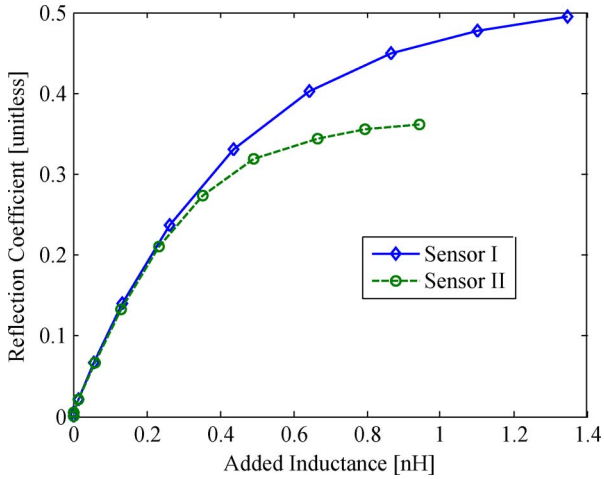

Fig. 9. Increase in the reflection coefficient with the added inductance.

A 0.2-mm crack width was chosen to start with in the simulations. The reasons for this setup are given as follows. First, the minimum crack width visible to the naked eye is in the range of 0.1–0.2 mm [17]. Second, in the modeling, the cable sensors in the crack region were meshed into cubicle cells of 0.05 × 0.05 × 0.05 mm, whereas a finer mesh leads to a significant demand on computational resources. Both sensors show strong TDR signals (approximately 0.065 in terms of reflection coefficient) with a minimum eye-visible crack width of 0.2 mm and a crack length of 0.6 turns; thus, this instance indicates that the proposed sensors can detect eye-invisible cracks (less than 0.2 mm), and the sensitivity of proposed sensors is much better than that of the other types of sensors mentioned in the Section I. It should be also mentioned that the full-wave FDTD tool has a limited capability of simulating sensitivity difference between two sensors in terms of the crack width. Thus, the sensitivity is further related to the maximum peak values of TDR signals. With a given crack width and length, a sensor with a higher reflection coefficient means that it has higher sensitivity. In this sense, Figs. 7 and 8 show that Sensor I has better sensitivity than Sensor II. One of the reasons is that Sensor I was made of a narrower (3-mm-wide) spiral than Sensor II, which results in a larger angle between the spiral separation and the axis of the sensor. This instance, in turn, causes a greater disturbance of the return current on the spiral-formed outer conductor. Under these circumstances, a greater added inductance is expected. Another reason is that the width and length of the spiral separation are directly associated with the crack width. When the crack is sufficiently wide, multiple turns of a spiral separation may present. For the same crack width, a sensor made of a narrower spiral may have a bigger spiral separation than the sensor made of a wider spiral, because it has a higher turn density per unit length. The higher value of spiral separation corresponds to a larger value of the added inductance and causes an increased reflection coefficient. Therefore, the sensor that is made of a 3-mm-wide spiral is expected to perform better. For both sensors under investigation, the reflection coefficient is plotted as a function of the added inductance, as shown in Fig. 9. The added inductance is evaluated using (3).

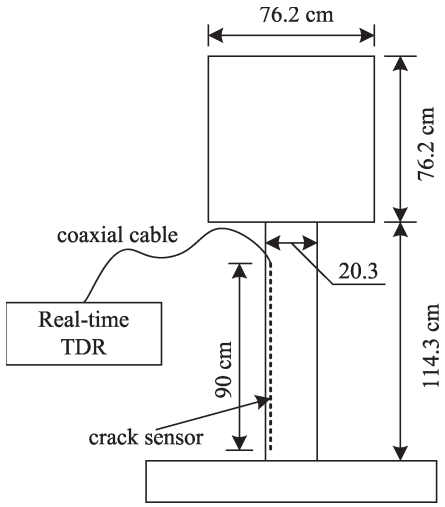

Fig. 10. Side view of the specimen and the test setup.

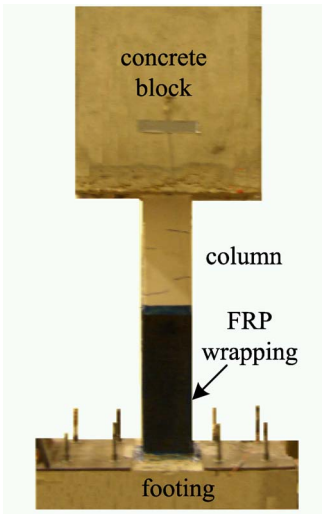

Fig. 11. Photo of the specimen.

III. Experimental Test

The performance of the proposed cable sensors was experimentally demonstrated and investigated for small-scale reinforced concrete beams under dynamic loading.

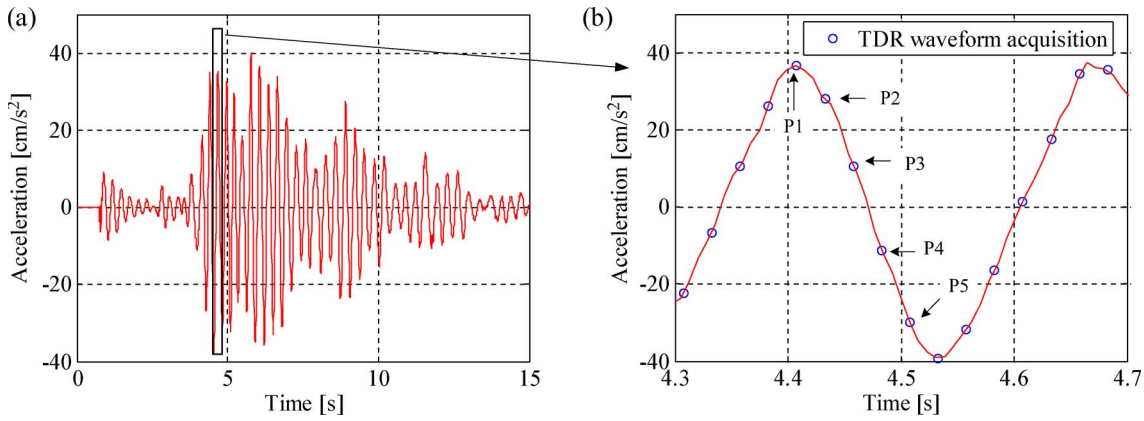

Fig. 12. Acceleration of the specimen (concrete block) during one test. (a) One complete acceleration waveform. (b) Waveform zoom-in and TDR acquisition points.

A. Test Specimen and Measurement Setup

The reinforced concrete column under test was designed as a 1/5 scale of a protocol column. Fig. 10 shows the geometry of the specimen and the measurement setup. One image of the specimen is presented in Fig. 11. The specimen consisted of a footing, a column, and a mass of concrete on the top of the column. The column was 114.3 cm in height and 20.3 cm × 20.3 cm in cross section. One 90-cm-long cable sensor was mounted near the surface of one face of the column. A cubical concrete block of 76.2 cm × 76.2 cm × 76.2 cm was cast on top of the column to simulate the superstructure mass of a bridge structure. The bottom half of the column was wrapped with a one-ply fiber-reinforced polymer (FRP) sheet. The footing was fixed on the unidirectional MTS shaking table, which was excited with the modified 1940 El Centro Earthquake ground motions. Fig. 12(a) shows the acceleration of the specimen (concrete block) during one test.

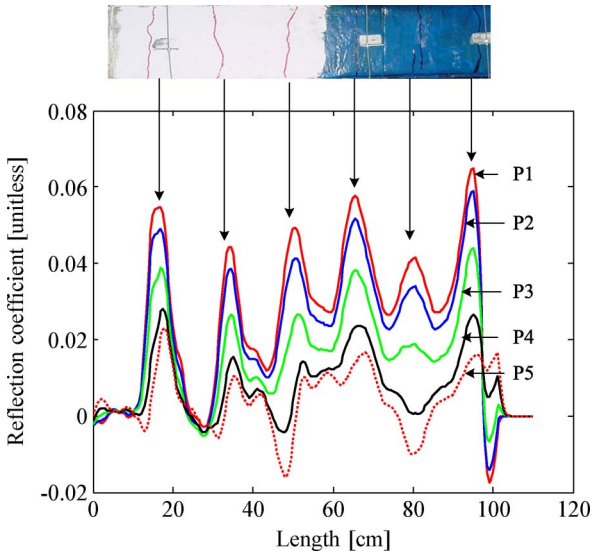

Fig. 13. Five TDR waveforms measured within a half cycle of the acceleration and a photo of the crack pattern on the column.

B. Sensor Performance

The sensor performance is assessed in terms of the crack localization and spatial resolution. A real-time TDR measurement setup was built for this test [18]. This instrument setup was set to allow 40 TDR signals acquisitions per second (with a 25-ms interval). As illustrated in Fig. 12(b), five TDR waveforms that were recorded within a half cycle of the acceleration waveform, which are denoted as P1, P2, P3, P4, and P5, were intentionally chosen, because the specimen was subjected to the maximum range of stress—from tension to compression. Accordingly, the crack sensor was subjected to a crack opening from maximum to zero.

Fig. 13 shows the measurement results, which convey not only the correlation between the measurement results and the crack pattern on the column but also the TDR signal evolvement with respect to the decreasing acceleration of the specimen. The six peaks of the TDR waveforms correlate well with the locations of all cracks observed on the column. This instance indicates that the sensor successfully identified all the cracks on the column. The spatial resolution of the sensor is approximately 5 cm. The spatial resolution can be improved. The signal loss that was introduced by the measurement setup, i.e., connecting cables, circuit network used for facilitating real-time measurements, is nonnegligible, but it can be reduced by optimizing the real-time TDR measurement system. Note that the cracks beneath the FRP sheet were actually hidden. Their presence was confirmed after the completion of the tests by peeling off the FRP sheet. The experiments show that the sensor can detect both surface and hidden cracks. According to the figure, the peak values at all crack locations generally decrease with a decreasing acceleration of the specimen. A larger crack can be expected at a higher acceleration of the specimen. Because of the dynamic nature of the excitation, it was impossible to measure the crack widths at these time instants. More investigations on the relation between the crack width and TDR waveform change will be addressed in Section IV.

IV. Automatic Fabrication Based on the Plasma-Spray Technique

The hand-soldered sensors demonstrated unavoidable nonuniformity and suffered from inconsistency of the performance due to its hand-made nature [19], [20]. To address these issues, a plasma-sprayed coating technology was employed instead of hand soldering to leverage sensor fabrication.

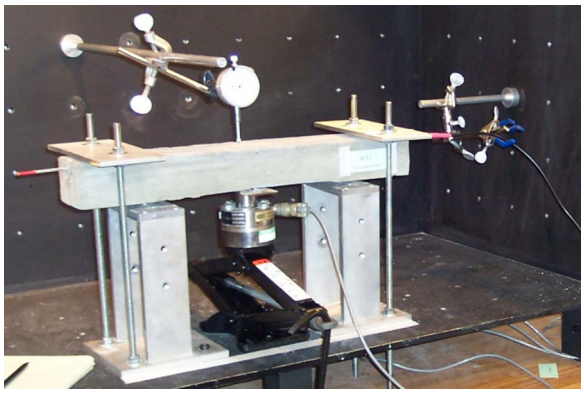

Fig. 14. Photo of a crack-controlled measurement setup.

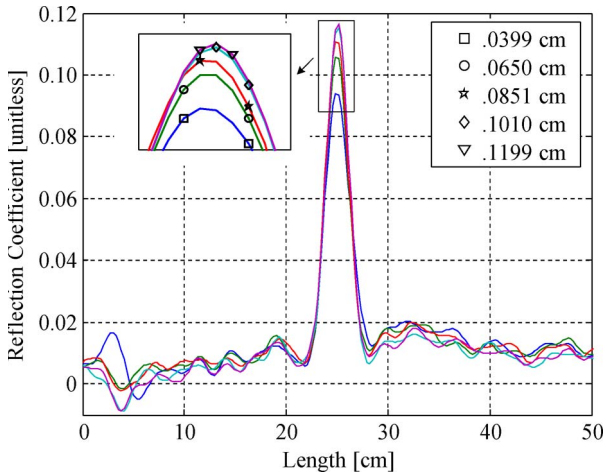

Fig. 15. TDR waveforms with increasing crack width for beam BF4.

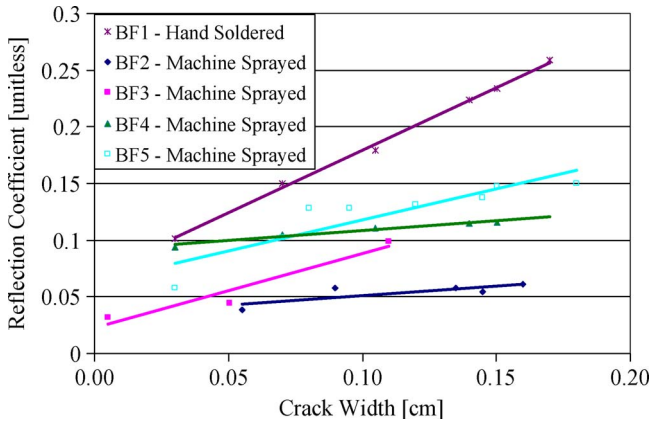

Fig. 16. TDR waveforms changes with respect to the crack width.

A. Implementation of Plasma-Sprayed Coating

The plasma-spray process is widely applied in the production of high-quality sprayed coatings [21]. The stainless steel spiral and the coating layer deposited on its surface form together an outer conductor of a sensor. A copper-based metallic powder was chosen because of its high conductivity and low cost. To have a good bonding between the coating layer and the substrate, the coating material needs to be in compression upon cooling. This condition requires the thermal expansion coefficient of the coating material to be less than that of the steel spiral. With the aforementioned requirements, several commercially available coating materials were tested. A pure copper (MetCo 55) was selected because of its overall performance. The powders were sprayed using a combination of primarily argon gas and small additions of hydrogen gas. During the spray process, additional cooling control was needed to avoid excessive oxidization of the coated metal material. The spray process was fine tuned to optimize the sensor coating in terms of the coating uniformity, coating adhesion to the steel spiral, and the electrical performance of the coated sensors. The sensors coated with a pure copper powder under the optimized process parameters were used in the laboratory-controlled measurements. With the plasma-spray coating technique, the machine-sprayed sensors demonstrated less than 0.010 reflection coefficient variations. As a comparison, the hand-soldered sensors typically have more than 0.050 reflection coefficient variation. The spray technique also provides mass production capability.

B. Performance of Coated Sensors

A controlled crack test was performed to further investigate the sensitivity of spray coating sensors and the correlation between the crack width and the reflection coefficient peak values. For this test, only one crack was introduced to the beam under test, and the crack width was gradually increased. Five sprayed sensors were individually grouted into 50-cm-long beams with cross sections of 6.4 cm $\times$ 7.6 cm. As shown in Fig. 14, the beam was simply supported at both ends and was tested under a concentrated load applied at midspan (three-point loading tests) using a car jack at 15-lb intervals. The crack width was measured with a Peak CS-100 Crackscope. A HP86100 oscilloscope with a TDR plug-in module was used to measure the sensor TDR response.

Five test specimens were designated with BF1 to BF5. The TDR waveforms measured from all beams had a clear peak that corresponds to the crack at the midspan of the beam. A set of the TDR reflected signals measured from the specimen BF4 at various loads are shown in Fig. 15. A 0.399-mm-wide crack suddenly appeared at a certain load level, and then, the crack width increased as the load level increased. The TDR waveforms captured this crack development, as shown in Fig. 15. Fig. 16 shows the peak values of the TDR waveforms versus the crack width for test specimens BF1–BF5. The initial crack that developed on specimen BF3 is 0.05 mm wide, which causes a reflection coefficient of 0.032. The initial crack widths for other three specimens are in the range of 0.4–0.6 mm. The sensors under test showed a sensitivity of detecting a 0.05-mm-wide crack. A test setup for better crack width control is under development to further test the sensitivity limit of the proposed sensors. The correlation between the crack width and the reflection coefficient for all five sensors under test are approximately linear within the range of tested crack widths. However, the sensitivity of the four plasma-sprayed sensors

varies in a considerable large range, which indicates that the consistency of coated sensors still needs further improvement. There are some possible reasons for the inconsistency. First, the bonding between the coating material and the spiral may vary from one sensor to another. Second, the bonding effect between concrete beams and sensors needs to be considered in the measurements or simulations, because, with the same crack width shown on the surfaces of different beams, the resulting spiral separation widths of sensors within corresponding beams may vary.

V. Engineering Implications

One critical implementation issue of coaxial cable sensors is the increasing signal loss as the length of cable sensors increases. The signal loss attenuates the signal magnitude and broadens the signal waveforms; thus, the sensitivity and spatial resolution of a distributed cable sensor are compromised. The primary factors that contribute to signal loss are the skin effect of the conductor, the dielectric loss, and the impedance mismatch loss due to discontinuities caused by the separation between the adjacent spirals. In this section, experiments and numerical simulations are combined to quantify individual loss components and their impact on the performance of the sensor. Design guidelines are given to reduce the signal loss and optimize the sensor design.

A. Signal-Loss Characterization

Two 1-m-long sensor prototypes were fabricated to quantify the contribution of each loss components, and a 1-m-long RG400 coaxial cable was used as a reference. The outer conductor of one sensor was made of a tin-plated stainless-steel spiral, and for the other sensor, the outer conductor was made of a gold-plated steel spiral. The thickness of the gold plating on the spiral was 0.025 mm. Two sensor prototypes were fabricated using a RG400 coaxial cable. The original outer conductor of a RG400 cable was peeled off, and then, a steel spiral or a gold-plated steel spiral was wrapped to the remaining inner conductor and the dielectric layer. The original outer conductor of the RG400 coaxial cable was made of double-shielded and braided silver-plated copper wires. Two cable sensors and the reference 1-m-long RG400 coaxial cable have the same type of inner conductor and dielectric insulation layer, and the only difference is the outer conductor; thus, the dielectric losses for three cable/sensors are the same. Thus, the skin-effect loss from outer conductors with different materials, e.g., a steel spiral, a gold-plated spiral, and a braided silver-plated copper wire (reference), can be quantified. The S_{21} of the two cable sensors and the reference RG400 cable were measured using a HP8753D vector network analyzer. Fig. 17 shows the magnitudes of S_{21} as a function of frequency. According to the figure, the gold-plated spiral substantially reduces the skin-effect loss at high frequencies compared with the steel spiral sensor. Impulse responses were obtained by transforming the S_{21} parameters into the time domain. As shown in Fig. 18, signal loss increases both the transition duration t_r and decay time t_d of the signals and reduces the amplitude of the signal compared to the original impulse. Herein, a concept of *peak loss* is introduced, and defined as in (4), shown at the bottom of the page.

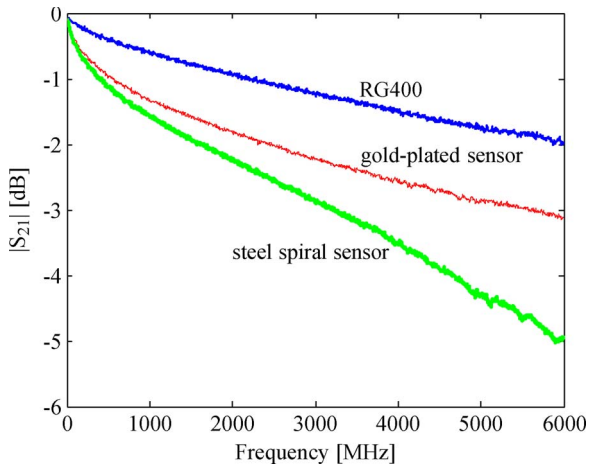

Fig. 17. Measured $|S_{21}|$ of two 1-m-long sensors and a 1-m-long RG400 coaxial cable.

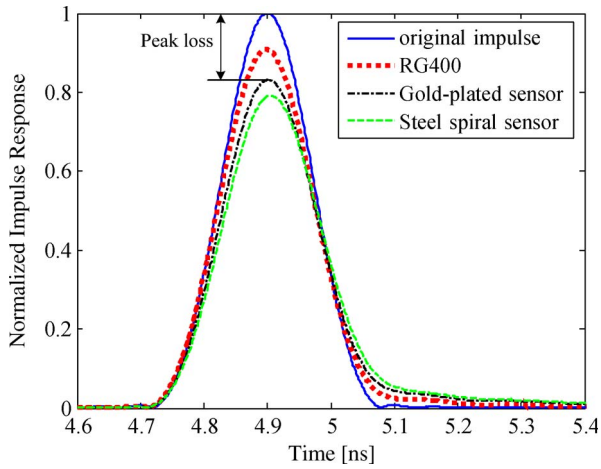

Fig. 18. Impulse responses of two 1-m-long sensors and the 1-m-long reference cable.

According to Fig. 18, the total peak loss of the reference cable, the gold-plated spiral sensor, and the steel spiral sensor are calculated as 9%, 17%, and 21%, respectively. The contributions of the skin effect and the dielectric loss, as well as the impedance mismatch loss, to the total peak loss are derived in the following sections.

$$Peak\ loss = \frac{Original\ signal\ magnitude - Attenuated\ signal\ magnitude}{Original\ signal\ magnitude} \times 100\% \tag{4}$$

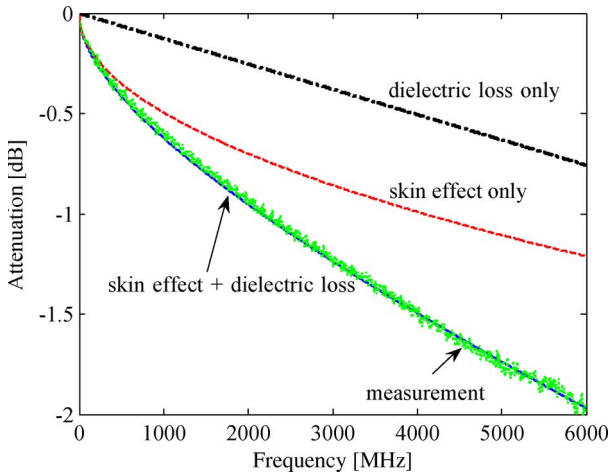

Fig. 19. Conductor and dielectric losses of the 1-m-long reference cable.

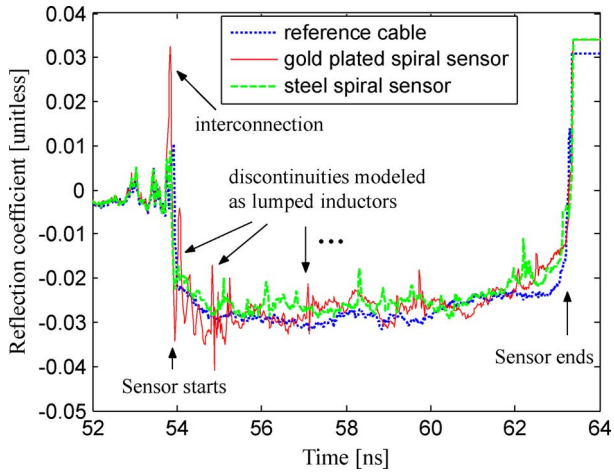

Fig. 20. Measured TDR waveforms of the two sensors and the reference cable.

1) Dielectric Loss: The dielectric layer between inner and outer conductors contributes to the signal loss. When the signal travels along the cable, a portion of the electric field energy is dissipated in the dielectric because of the polarization of dielectric material dipoles by the electric field. For almost nondispersive bulk dielectrics, the dielectric loss is directly proportional to the frequency. Such dielectrics as polyethylene and Teflon, which are typically used for the manufacturing of flexible cables, exhibit low dielectric loss at frequencies below a few gigahertzes.

The transition duration t_r of the step pulse signal launched from a common TDR device is on the order of 30 ps, with a corresponding signal bandwidth of 11.7 GHz. Although the dielectric material used in the sensors is a low-loss polyethylene, the dielectric loss at high frequencies still cannot be ignored for such a wideband signal. To estimate the dielectric loss, a transfer function of a transmission line was employed [22]. We have

$$H(f) = e^{-k_s\sqrt{f}} \times e^{-k_d f} \tag{5}$$

where k_s is a constant for the skin effect, k_d is a constant for the dielectric loss, and f is the frequency. The attenuation is calculated as

$$\text{Attn./dB} = 20 \cdot \log|H(f)| = 20 \cdot \log|e^{-k_s\sqrt{f}-k_d f}|. \tag{6}$$

Since the impedance mismatch loss is negligible for the reference cable, (6) can be used to determine k_s and k_d for quantifying the conductor and dielectric losses. By optimizing k_s and k_d, the curve calculated with (6) matches with the measurement result well, as shown in Fig. 19. By transforming the frequency-domain attenuation data into the time domain, the dielectric loss and the skin-effect contributions to the total peak loss were calculated as 3% and 6%, respectively. Note that the dielectric losses for the three cables are the same.

2) Skin Effect and Impedance Mismatch Loss: Both skin effect and the impedance mismatch contribute to the peak loss for the two hand-made cable sensors. Skin effect has a greater effect on the high-frequency part of a signal spectrum than on the low-frequency components [14], [23]. As the frequency increases, the current trends to concentrate on the surface of the conductor within a skin depth. The effective cross-sectional area of the conductor becomes smaller. Therefore, the per-unit-length resistance of a conductor increases with frequency, and in the first-order approximation, it is proportional to the square root of the frequency.

The impedance mismatch, which results in multiple signal reflections, is primarily attributed to the manual fabrication effect of the sensors. Even very narrow gaps between two consecutive spirals may cause unnegligible local characteristic impedance variations of the cable sensors. When a signal encounters these gaps, a portion of the signal will be reflected back. Hence, the resulting transmitted signal level reduces. The measured TDR waveforms of the two cable sensors, as well as of the reference cable, are shown in Fig. 20. Although the two sensors were well fabricated, many small discontinuities are still seen on TDR waveforms. The impedance variation of the two sensors, particularly the gold-plated spiral sensor, is obviously larger than that of the reference cable.

The skin effect and impedance mismatch losses cannot easily be separated and quantified with experiments; thus, a numerical SPICE model was used to quantify two effects. The basic properties of the sensors were modeled as lossless transmission line elements. The spikes caused by the fabrication artifacts were modeled as lumped inductors, whose values were measured with a TDR [24]. The skin-effect loss was represented with an R–L ladder circuit model [25]. When the inductors, which represent the discontinuities, were removed from the SPICE model, the peak loss changed. This difference in the peak loss for the gold-plated sensor is approximately 5%, which is contributed by the impedance mismatch effect. The values of the total peak loss, the peak loss due to the dielectric, and the loss due to the impedance mismatch for the gold-plated sensor are known (i.e., they are 17%, 3%, and 5%, respectively); thus, the peak loss due to the skin effect is the remaining, which is 9%. In the same way, the impedance mismatch loss and the skin-effect loss for the steel spiral sensor are calculated as 1% and 17%, respectively. The skin-effect-induced peak loss can also be calculated by removing the R–L ladder skin-effect model from the original SPICE model.

TABLE II
CONTRIBUTIONS OF THREE LOSS MECHANISMS TO THE TOTAL PEAK LOSS

	Skin effect	Dielectric loss	Reflection loss	Total loss
Gold-plated spiral sensor	9 %	3%	5%	17%
Steel spiral sensor	17 %	3%	1%	21%
Reference cable	6 %	3%	0%	9%

Table II summarizes the contributions of the three loss components to the total peak loss. Several conclusions can be drawn according to the data in this table.

1) Skin effect is a dominant factor in the signal loss. Using a high-conductivity metal for the inner conductor and the outer shield of a cable sensor can significantly reduce the signal loss.
2) The dielectric loss can be well controlled within a wide frequency range from dc to 6 GHz by using a low lossy dielectric material, e.g., polyethylene or Teflon, as the insulation layer of a cable sensor.
3) The impedance mismatch loss highly depends on the fabrication quality of a cable sensor. A controlled fabrication process is necessary to minimize this effect.

B. Spatial Resolution and Sensitivity

Spatial resolution is defined as the minimum distance between two adjacent cracks that can be resolved by a crack sensor. For two pulses with equal amplitudes in the time domain, the spatial resolution is approximately 50% of the impulse width [26] and can be calculated as

$$\Delta l = |l'_{0.5} - l''_{0.5}| \tag{7}$$

where $l'_{0.5}$ is the location of the point on the left pulse edge whose magnitude is 50% of the peak value, and $l''_{0.5}$ is the location of the point on the right pulse edge whose magnitude is 50% of the peak value.

Sensitivity is defined as the minimum width of a crack that a sensor can detect. As shown in Section IV, a crack on the concrete beam surfaces with a width as low as 0.05 mm was successfully captured. The noise floor of a TDR with 16 waveforms, on the average, is approximately 0.003 in terms of the reflection coefficient [20]. To successfully distinguish the TDR signal from the noise floor, the limit of the reflection coefficient that results from a crack is set to be twice the noise floor, which is 0.006. Because the signal loss attenuates the amplitude of the signal and broadens the waveforms, a TDR signal can be buried in the noise floor due to the signal attenuation. The signal loss increases along the sensor; thus, the sensitivity and the spatial resolution of a sensor decrease along the sensor. For a given crack, a higher reflection coefficient leads to a higher sensitivity of the sensor.

The signal-loss effect is a function of the sensor length. It can be obtained by convolving the input signal with the impulse response of a sensor. The lossless transmission line model of a cable sensor, as shown in Fig. 3, was used to generate a TDR waveform of a sensor with a crack. The characteristic impedance of the sensor is 50 Ω. The lumped inductor is 1 nH. The excitation is a step pulse with a bandwidth of 6 GHz, which is the integration of the measured original impulse response over time. The bandwidth of the step pulse is the same as the bandwidth of the impulse response of the sensors. A spike that results from the 1-nH inductor is shown in Fig. 21 and is labeled as the original pulse. By convolving the original pulse with the measured impulse response of the 1-m-long steel spiral sensor multiple times, the original pulse is attenuated by lossy steel spiral sensors of different lengths. Fig. 21 shows a series of distorted waveforms.

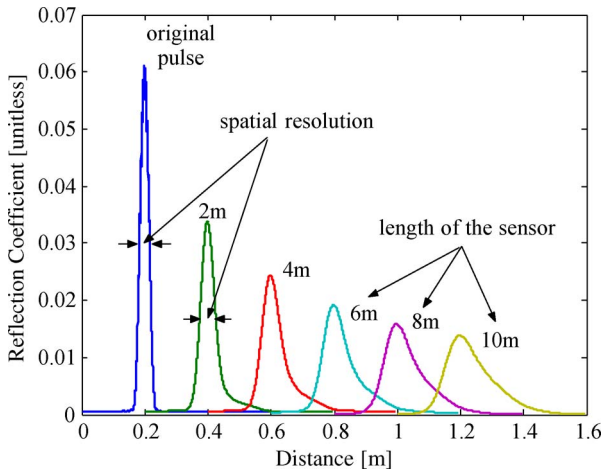

Fig. 21. Output signals of the steel spiral sensor with different lengths when excited with the original pulse.

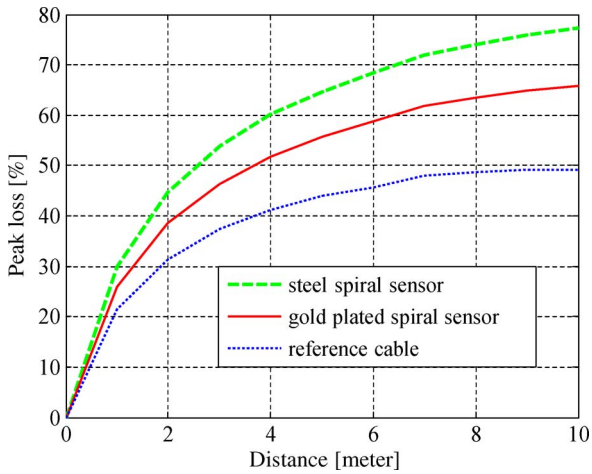

Fig. 22. Peak loss of the two sensors and the reference cable with different lengths.

The impact of the signal loss on the sensitivity of the steel spiral sensor is investigated through the peak loss. A sensor with a higher reflection coefficient means that it has higher sensitivity. For a given crack, a TDR easily detects a sensor with a higher reflection coefficient. In addition, the more sensitive sensor can sustain more signal loss. Fig. 22 shows that the peak loss exponentially increases with the length of the sensor, and this figure can be used to determine the sensor's useful

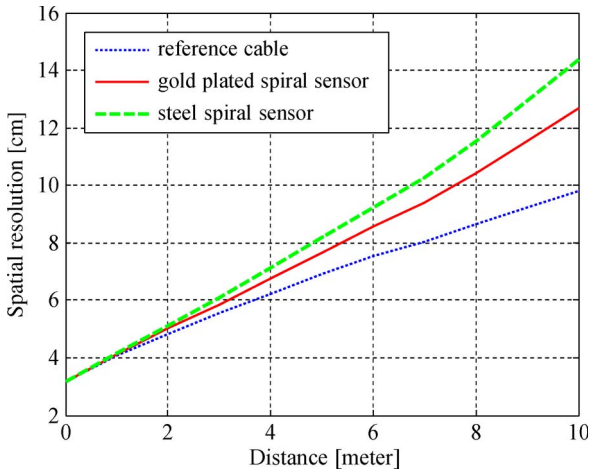

Fig. 23. Spatial resolution of two sensors and the reference cable with different lengths.

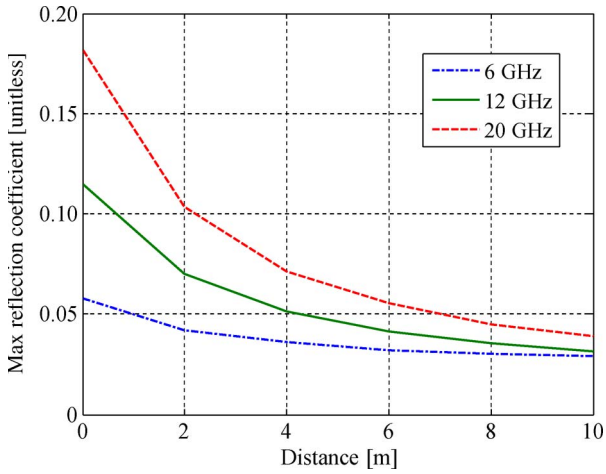

Fig. 24. TDR signal peak value as a function of the sensor length when excited with three pulses with different bandwidths.

length and sensitivity. For example, if the reflection coefficient is 0.020 for a 0.03-mm-wide crack and the peak loss is 70% for a 6.4-m-long steel spiral sensor, then, according to Fig. 22, the attenuated peak value of the signal is $0.020 \times (1-70\%) = 0.006$. This value is twice as much as the TDR measurement noise floor. The sensitivity of the steel spiral sensor at 6.4 m is a 0.03-mm-wide crack, and the corresponding maximum useful length of this sensor is limited to 6.4 m.

Signal loss limits the useful length of a sensor, but signal processing techniques can significantly extend the useful length. For example, the information of the peak loss with respect to the sensor length can be used to compensate for the magnitude attenuation. Given the crack locations, the peak loss can be estimated from the corresponding peak loss curve. The actual amplitude of the pulses can be evaluated as

$$\textit{Compensated pulse amplitude} = \frac{\textit{recorded pulse amplitude}}{1 - \textit{peak loss}(\%)}. \quad (8)$$

Using (2), the added inductance can be calculated with the compensated peak values, and then, the added inductance can further be related to the size of a crack.

The spatial resolution as a function of the sensor length is calculated using (7). The results are shown in Fig. 23. When exciting a steel spiral sensor by a step pulse with a bandwidth of 6 GHz, the spatial resolution decreases from 3.2 cm at zero length (lossless) to 14.4 cm at the 10-m length. By decreasing the transition duration of the step pulse launched by a TDR, the spatial resolution can be improved. However, this improvement is limited by the sensor length. The reason will be discussed in the following section.

C. Sensor Design Optimization

Many parameters influence the performance of a sensor. The important parameters that directly influence sensitivity, spatial resolution, and peak loss of a given sensor are not only the skin effect, the dielectric loss, and the impedance mismatch loss but also the impedance of the sensor and the transition duration of the step function launched with the TDR.

Equation (2) indicates that the maximum reflection coefficient of a sensor is inversely proportional to the transition duration t_r. However, there is a limit for reducing the transition duration t_r, because a pulse with a smaller transition duration corresponds to a wider frequency spectrum. The coaxial cable sensor effectively acts as a low-pass filter. Longer sensors have lower frequency bandwidth compared with shorter sensors. When a cable sensor is substantially long, the performance of the sensor will no longer benefit from a faster TDR because of the limited bandwidth of the cable sensor. To investigate the suitable bandwidth of a TDR step function pulse, the impulse responses of the 1-m-long reference cable were measured with a vector network analyzer for three different bandwidths: 1) 30 kHz–6 GHz; 2) 50 MHz–12 GHz; and 3) 50 MHz–20 GHz. As described in Section V-A, three TDR waveforms of a lossless sensor with 1-nH lumped inductor excited with 6-, 12-, and 20-GHz-bandwidth step functions were obtained. By convolving these three impulse responses of the cable with the TDR waveforms, the TDR signal peak values of the sensor excited with step functions with different bandwidths can be evaluated with respect to the sensor length. Fig. 24 shows that, with a step function of a wider spectrum, the peak values of TDR signals decay much faster along the sensor length compared to that with a lower bandwidth step function. At a 10-m length, three curves tend to converge. If a sensor has a higher signal loss, three curves may converge before 10 m. A TDR with a 6-GHz-bandwidth step function spectrum may be a suitable choice for sensor applications because of the compromise between the instrument cost and the sensitivity of the sensors. The corresponding transition duration of the step function is approximately 60 ps.

The reflection coefficient of the sensor is also inversely proportional to the sensor impedance, as shown in (2). Small characteristic impedance is preferable for higher sensor response. However, the sensor with 50 Ω impedance has the lowest signal loss [14]. The suitable characteristic impedance of a sensor is a compromise between the maximum TDR signals and the signal loss.

VI. Conclusion

A prototype cable sensor based on the topology modification of the outer conductor has been developed to improve its sensitivity. The experimental results have shown that a single distributed coaxial cable sensor can capture most of the cracks that were intercepted by the sensor. The distributed feature of the TDR sensing technique makes a cable sensor very promising for applications related to identifying the profile of a crack pattern in reinforced concrete structures. The distributed cable sensor is 10 times more sensitive to a crack development than a traditional cable sensor.

Signal losses in a cable sensor comprised of three components: 1) skin effect; 2) dielectric loss; and 3) impedance mismatch. The impact of the signal loss on the sensitivity and spatial resolution of a sensor was quantified with experiments and numerical simulations. The skin effect, i.e., conductor loss, was dominant and can significantly be reduced by using a metal with a high conductivity for both the inner conductor and the outer shield of a cable sensor. Manual fabrication may introduce artifacts that cause unintentional multiple signal reflections. An automated and controlled fabrication process can minimize this effect. By selecting a low lossy dielectric material as the insulation layer of a cable sensor, e.g., polyethylene or Teflon, the dielectric loss can be well controlled within a wide frequency range. In addition, the peak-loss-compensation approach was proposed to enhance the sensor performance.

The new plasma-spray coating technique can significantly improve the uniformity of the sensor. This manufacturing technique moves the emerging technology one step further toward practical applications. With plasma-sprayed sensors, the experimental results show that the peak reflection coefficient from a local crack is linearly proportional to the width of the crack, at least in the range of measurements.

References

[1] E. P. Small, "Condition of the nation's highway bridges," *TR News*, vol. 194, pp. 3–8, 1998. Transportation Research Board.

[2] S. W. Doebling, C. R. Farrar, M. B. Prime, and D. W. Shevitz, "Damage identification and health monitoring of structural and mechanical systems from changes in their vibration characteristic: A literature review," Los Alamos Nat. Lab., Los Alamos, NM, Tech. Rep. LA-13070-MS, 1996.

[3] G. Chen, X. Yang, H. Mu, and A. Nanni, "Nonlinear vibration signatures as effective tools for damage detection of reinforced concrete members," in *Proc. 3rd Int. Workshop Structural Health Monitoring*, Sep. 2001, p. 594.

[4] F. Ansari, "Fiber optic health monitoring of civil structures," in *Proc. 1st Int. Conf. Structural Health Monitoring Intell. Infrastructures*, Tokyo, Japan, Nov. 2003, vol. 1, pp. 19–30.

[5] A. Brown, M. DeMerchant, X. Bao, and T. W. Bremner, "Analysis of the precision of a Brillouin scattering based distributed strain sensor," in *Proc. 6th SPIE Int. Symp. Smart Structures Mater.*, 1999, vol. 3670, pp. 359–365.

[6] X. Gu, Z. Chen, and F. Ansari, "Embedded fiber optic crack sensor for reinforced concrete structures," *ACI Struct. J.*, vol. 97, no. 3, pp. 468–476, 2000.

[7] Z. S. Wu, T. Takahashi, and K. Sudou, "An experimental investigation on continuous strain and crack monitoring with fiber optic sensors," *Concrete Res. Technol.*, vol. 13, no. 2, pp. 139–148, 2002.

[8] Z. S. Wu and B. Xu, "Infrastructural health monitoring with BOTDR fiber optic sensing technique," in *Proc. 1st Int. Workshop Structural Health Monitoring Innovative Civil Eng. Structures*, 2002, pp. 217–226.

[9] Y. Zhao and F. Ansari, "Quasi-distributed white light fiber optic strain sensor," *Opt. Commun.*, vol. 196, no. 1–6, pp. 133–137, Sep. 2001.

[10] M. Su, "Quantification of cable deformation with time-domain reflectometry techniques," Ph.D. dissertation, Northwestern Univ., Chicago, IL, 1997.

[11] M. W. Lin, A. O. Abatan, and W. Zhang, "Crack damage detection of concrete structures using distributed electrical time-domain reflectometry (ETDR) sensors," in *Proc. SPIE Smart Structures Mater.—Smart Syst. Bridges, Structures, Highways*, 1998, vol. 3325, pp. 173–180.

[12] M. W. Lin, A. O. Abatan, and Y. Zhou, "High sensitivity electric TDR distributed strain sensor," in *Proc. 7th SPIE Int. Symp. Smart Structures Mater.*, Newport Beach, CA, Mar. 5–9, 2000, vol. 3986, pp. 463–471.

[13] S. Sun, D. Pommerenke, J. L. Drewniak, and G. D. Chen, "Signal loss, spatial resolution, and sensitivity of long coaxial crack sensors," in *Proc. 11th SPIE Annu. Symp. Smart Structures Mater.*, 2004, pp. 786–797.

[14] D. M. Pozar, *Microwave Engineering*, 2nd ed. New York: Wiley, 1998.

[15] H. Mu, "Development and validation of coaxial cable sensors for damage detection of reinforced concrete structures," Ph.D. dissertation, Univ. Missouri-Rolla, Rolla, MO, 2003.

[16] E. Bogatin, *Signal Integrity—Simplified*. Upper Saddle River, NJ: Prentice-Hall, 2004.

[17] M. Richardson and R. Mark, *Fundamentals of Durable Reinforced Concrete*. New York: Taylor & Francis, 2002.

[18] G. D. Chen, L. Xue, D. Pommerenke, X. Huang, and J. L. Drewniak, "Real-time monitoring of seismic performance of RC structures with distributed crack sensors and high-speed measurement system," in *Proc. 5th Int. Workshop Structural Health Monitoring*, 2005, pp. 1274–1281.

[19] G. Chen, H. Mu, D. Pommerenke, and J. L. Drewniak, "Damage detection of reinforced concrete beams with novel distributed crack/strain sensors," *Struct. Health Monit.*, vol. 3, no. 3, pp. 225–243, 2004.

[20] G. Chen, S. Sun, D. Pommerenke, J. Drewniak, G. Greene, R. D. McDaniel, A. Belarbi, and H. Mu, "Crack detection of a full-scale reinforced concrete girder with a distributed cable sensor," *Smart Mater. Struct.*, vol. 14, no. 3, pp. S88–S97, May 2005.

[21] [Online]. Available: http://www.gordonengland.co.uk/ps.htm

[22] W. Humann, "Compensation of transmission line loss for Gb/s test on ATEs," in *Proc. Int. Test Conf.*, Oct. 7–10, 2002, pp. 430–437.

[23] N. S. Nahman, "A discussion on the transient analysis of coaxial cables considering high-frequency losses," *IRE Trans. Circuit Theory*, vol. 9, no. 2, pp. 144–152, Jun. 1962.

[24] D. J. Dascher, "Measure Parasitic Capacitance and Inductance Using TDR," Agilent Technol., Santa Clara, CA, 2002. App. Notes.

[25] B. K. Sen and R. L. Wheeler, "Skin effect models for transmission line structures using Generic SPICE circuit simulators," in *Proc. IEEE 7th Top. Meet. Elect. Perform. Electron. Packag.*, Oct. 26–28, 1998, pp. 128–131.

[26] *Agilent 8753D Vector Network Analyzer Manual*, Agilent Technol., Santa Clara, CA, 1997.

Shishuang Sun (S'03–M'07) received the B.S. and M.S. degrees in electrical engineering from Shanghai JiaoTong University, Shanghai, China, in 1999 and 2002, respectively, and the Ph.D. degree in electrical engineering from the University of Missouri, Rolla, in 2006.

He is currently a member of Technical Staff with the Product Characterization Group, Altera Corporation, San Jose, CA. His research interests include signal integrity in high-speed digital systems and power delivery network design and modeling.

David J. Pommerenke (M'98–SM'03) was born on April, 11, 1962 in Ann Arbor, MI. He received the Diploma in electrical engineering and the Ph.D. degree in transient fields of electrostatic discharge (ESD) from the Technical University of Berlin, Germany, in 1989 and 1995, respectively.

In 1989, he was a Research and Teaching Assistant of electromagnetic compatibility (EMC) and high-voltage engineering with the Technical University of Berlin. In 1996, he joined Hewlett Packard. In 2001, he was an Associate Professor with the EMC Laboratory, Department of Electrical and Computer Engineering, Missouri University of Science and Technology (MS&T; formerly known as the University of Missouri, Rolla). He is also a member of working group that sets the ESD standards. His research interests are EMC, ESD, numerical modeling, high-voltage partial discharge detection systems, and design of electronic test and measurement equipment.

James L. Drewniak (S'85–M'90–SM'01–F'07) received the B.S., M.S., and Ph.D. degrees in electrical engineering from the University of Illinois, Urbana-Champaign, in 1985, 1987, and 1991, respectively.

In 1991, he joined the Department of Electrical Engineering, Missouri University of Science and Technology (MS&T; formerly known as the University of Missouri-Rolla), Rolla, where he is currently a Faculty Member in the EMC Laboratory. His research and teaching interests include electromagnetic compatibility in high-speed digital and mixed-signal designs, signal and power integrity, electronic packaging, electromagnetic compatibility in power electronic based systems, electronics, and antenna design.

Dr. Drewniak is an Associate Editor for the IEEE TRANSACTIONS ON ELECTROMAGNETIC CAPABILITY.

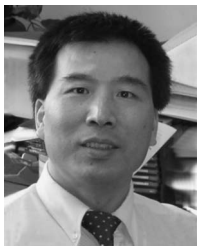

Genda Chen received the M.S. degree from Dalian University of Technology, Dalian, China, in 1985, and the Ph.D. degree from the State University of New York at Buffalo, New York, in 1992.

From 1993 to 1996, he was with Steinman Consulting Engineers. Since 1996, he has been with the Department of Civil, Architectural, and Environmental Engineering, Missouri University of Science and Technology (MS&T; formerly known as the University of Missouri-Rolla), Rolla. He is currently a Professor of civil engineering and serves as the Interim Director of the Center for Infrastructure Engineering Studies. He is a member of the Editorial Board of *Structural Control and Health Monitoring*. Recently, he has been a Guest Editor of a special issue of *Structural Engineering and Mechanics*. He is the author of more than 150 papers, including more than 40 journal articles. His research interests include dynamic response reduction with supplemental damping and control devices, damage detection and structural health monitoring, and earthquake hazard assessment and mitigation of civil infrastructure.

Dr. Chen is a registered Professional Engineer in the State of California. He is a Fellow of the American Society of Civil Engineers (ASCE) and a member of the Earthquake Engineering Research Institute and the International Society for Structural Health Monitoring of Intelligent Infrastructure. He received the prestigious Faculty Early Career Development Award (CAREER) from the U.S. National Science Foundation in 1998. He has served on the organization and program committees of more than 10 national and international conferences. He has recently become the Secretary of ASCE Structural Control Committee.

Liang Xue (S'06–M'07) received the B.S. degree in electrical engineering from Tsinghua University, Beijing, China, in 2003, and the M.S. degree in electrical engineering, with specialization in high-speed system design and signal integrity, from the Missouri University of Science and Technology (MS&T; formerly known as the University of Missouri-Rolla), Rolla, in 2006.

From 2006 to 2008, he was a Signal Integrity Engineer with the National Semiconductors. He is currently with the VLSI Department, Nvidia Corporation, Santa Clara, CA, as a Signal Integrity Engineer.

Michael A. Brower received the B.S. and M.S. degrees from the Missouri University of Science and Technology (MS&T; formerly University of Missouri-Rolla), Rolla, in 2005 and 2008, respectively.

Since 2006, he has been an Assistant Structural Engineer with the Burns and McDonnell Engineering Company, Kansas City, MO. His research interest is focused on the implementation issues of distributed coaxial cable crack sensors embedded in reinforced concrete members.

Marina Y. Koledintseva (M'96–SM'03) received the M.S. degree (*summa cum laude*) and the Ph.D. degree from the Moscow Power Engineering Institute (Technical University) [MPEI(TU)], Moscow, Russia, in 1984 and 1996, respectively.

From 1983 to 1999, she was an Engineer, a Research Associate, and a Senior Scientist with the Ferrite Laboratory, MPEI(TU), where she combined research with teaching as an Associate Professor from 1997 to 1999. In January 2000, she came to the U.S. as a Visiting Professor and joined the EMC Laboratory, Department of Electrical and Computer Engineering, Missouri University of Science and Technology (MS&T; formerly University of Missouri-Rolla), Rolla, where she has been a Research Professor since 2005. She is the author of about 150 papers and seven inventions. Her research interests include microwave engineering, interaction of electromagnetic field with ferrites and composite media, their modeling, and application for electromagnetic compatibility.

Dr. Koledintseva is a member of the Education, TC-9 Computational Electromagnetics, and TC-11 (Nanotechnology) Committees of the IEEE Electromagnetic Compatibility Society.